Geochronology, 6, 313–323, 2024
https://doi.org/10.5194/gchron-6-313-2024

GEOCHRONOLOGY Open Access EGU

Short communication: Inverse correlation between radiation damage and fission-track etching time on monazite

Toru Nakajima[1], **Shoma Fukuda**[1], **Shigeru Sueoka**[1], **Sota Niki**[2], **Tetsuo Kawakami**[3], **Tohru Danhara**[4], **and Takahiro Tagami**[3]

[1]Tono Geoscience Center, Japan Atomic Energy Agency, Toki, 509-5102, Japan
[2]Geochemical Research Center, University of Tokyo, Tokyo, 113-0033, Japan
[3]Department of Geology and Mineralogy, Kyoto University, Kyoto, 606-8502, Japan
[4]Kyoto Fission-Track Co., Ltd., Kyoto, 603-8832, Japan

Correspondence: Toru Nakajima (nakajima.toru@jaea.go.jp)

Received: 26 January 2024 – Discussion started: 21 February 2024
Revised: 2 May 2024 – Accepted: 9 May 2024 – Published: 3 July 2024

Abstract. In this study, we explored the impacts of radiation damage and chemical composition on the etching time of fission tracks in monazite. Despite the potential of monazite fission-track (MFT) dating as an ultralow-temperature thermochronology, the comprehensive effects of radiation damage and non-formula elements, especially on the etching rate of MFTs, remain unexplored, and established analytical procedures are lacking. We quantified the degree of radiation damage (Δ_{FHWM}) in Cretaceous to Quaternary monazites distributed in the Japan arc through Raman spectroscopy and chemical composition analyses. Subsequently, MFT etching was performed to examine the correlation between these parameters and the etching time.

Estimation of the degree of radiation damage showed an increase in radiation damage corresponding to the cooling age of each geological unit. For example, the Toya ignimbrite (ca. 0.1 Ma) and the Kurobegawa granodiorite (< 0.8 Ma), both of which are types of monazite from Quaternary geological units, have Δ_{FHWM} values of 0.27 and 0.55 cm^{-1}, respectively. In contrast, the Muro ignimbrite (ca. 15 Ma) has a Δ_{FHWM} value of 4.01 cm^{-1}, while the Kibe granite and the Sagawa granite, both of which are Cretaceous granitoids, yielded 7.35 and 6.31 cm^{-1}, respectively. MFT etching of these samples according to the existing recipe (6 M HCl at 90 °C for 60–90 min) was completed at 1200, 860, 210, 120, and 90 min for the Toya ignimbrite, Kurobegawa granodiorite, Muro ignimbrite, Sagawa granite, and Kibe granite, respectively. These outcomes highlight an inverse relationship between MFT etching time and the degree of radiation damage in monazite, while the correlation between MFT etching time and chemical composition was unclear. The results affirm earlier considerations that the etching rate of MFTs is strongly influenced by radiation damage. Conversely, young samples with lower levels of radiation damage exhibit higher chemical resistance, suggesting that existing etching recipes may not adequately etch MFTs.

1 Introduction

Monazite (LREE(PO_4)) commonly contains U and Th and is therefore considered a potential target for fission-track (FT) dating. In recent years, annealing experiments on Cf fission fragment tracks have indicated that the closure temperature of the monazite fission-track (MFT) system ranges from 25–45 °C on the geological timescale (10^6–10^7 years; Jones et al., 2021). With ongoing advancements in analytical methodologies and an increasing understanding of the annealing kinetics of MFTs, the MFT system is expected to become a powerful tool for approaching the thermal history of ultralow temperature ranges (< 50 °C). Moreover, owing to the typically high U and Th concentrations (> 1000 ppm) in monazite, MFT dating is anticipated to be applicable to the dating of rocks that formed and/or cooled after the Quaternary period.

Despite these optimistic prospects, numerous unresolved details remain in the experimental procedures of MFT dating at present. For example, MFT etching characteristics

have not been sufficiently explored. Since the FT (daughter) formed by the spontaneous fission of radionuclides (parents) cannot be observed optically (latent tracks; Paul and Fitzgerald, 1992), it is necessary to selectively etch the FTs for dating measurements (Fleischer and Price, 1964). Inconsistency in the degree of etching progression can lead to biases in counting and length measurements of FTs when using an optical microscope (e.g., Laslett et al., 1984; Ketcham et al., 2015; Tamer et al., 2019; Tamer and Ketcham, 2020). Therefore, the etching protocols of zircon and apatite FTs have been carefully investigated to ensure robust dating and thermal analysis (Laslett et al., 1982; Green, 1988; Yamada et al., 1993, 1995). However, variations in FT etching rates are commonly observed within the same sample at inter- and intra-grain levels for conventional FT dating methods (e.g., apatite, zircon, and titanite), and factors governing etching rates and subsequent etching protocols based on these factors have been proposed. For apatite, differences in chemical resistance result from its chemical composition, particularly the F–Cl–OH contents (e.g., Burtner et al., 1994), leading to varying FT etching rates. On the other hand, for zircon, there is a well-known relationship in which etching time and FT density ($\propto$ U concentration) inversely correlate within the same sample (e.g., Gleadow et al., 1976), reflecting the decrease in chemical resistance due to accumulated radiation damage.

It is widely known that MFTs can be etched using HCl. Jones et al. (2019) showed that MFTs can be etched within a certain duration under controlled temperature (6 M HCl at 90 °C for 60–90 min), and subsequent studies have employed this etching condition (Jones et al., 2021, 2023). Similar to other minerals used in FT dating, previous studies have found inter-grain differences in etching rates for monazite, attributed to variations in U and Th concentrations and the resulting accumulation of radiation damage (Fayon, 2011; Jones et al., 2019). In previous studies, only aged monazites, such as the Antsirabe monazite (ca. 500 Ma) and the Harcourt monazite (ca. 370 Ma), were used in experiments (Weise et al., 2009; Jones et al., 2019). Although some experiments have pre-annealed spontaneous tracks and radiation damage (Weise et al., 2009; Jones et al., 2019, 2021), the actual effects of radiation damage remain largely unexplored. In particular, younger (Cenozoic) monazites may lack significant radiation damage and may resist existing MFT etching techniques. Additionally, considering that monazite is a phosphate with various compositions, similar to apatite, the influence of chemical composition on etching rates should be noted.

In this study, five monazites with various levels of radiation damage were collected in order to primarily investigate the effect of radiation damage on FT etching time. The formation ages of the host rocks range from the Cretaceous to the Quaternary. For these monazites, we determined (1) the chemical composition, (2) the degree of accumulated radiation damage, and (3) the MFT etching time. This paper reports an inversely proportional relationship between MFT etching time and radiation damage and discusses the MFT etching protocols for young monazites.

2 Sample description

2.1 The Toya ignimbrite (Toya-5b)

The Toya ignimbrite, a siliciclastic eruptive deposit, is distributed in the western region of Hokkaido, Japan (Fig. 1a and b). Predominantly comprised of pumiceous beds and lag deposits, it originates from the catastrophic eruption of the Toya caldera at ca. 0.1 Ma (reviewed by Tomiya and Miyagi, 2020). Along the Osaru River, the Toya ignimbrite is subdivided into units 1–6, which are interpreted to have been deposited by pyroclastic flows during a series of intermittent catastrophic eruptions (Goto et al., 2018). The monazite sample employed in this study was separated from the unit 5b pumice. Niki et al. (2022) documented a zircon and monazite U–Th disequilibrium age of $113.8^{+5.4}_{-5.2}$ ka (95 % confidence levels) from the unit 5b pumice. The outcrop from which the sample (Toya-5b) was collected exhibits a plateau with no overlying layers other than the Kt-2 tephra, which erupted from the Kuttara volcano in southwestern Hokkaido (ca. 40 ka; Yamagata, 1994). Toya-5b yields euhedral and colorless monazite (Fig. 2a), which includes numerous glassy melt inclusions along with vapor. The internal microstructure is not clearly identified in backscattered electron (BSE) images, indicating a very homogeneous intra-grain composition (Fig. 2b).

2.2 The Kurobegawa granodiorite (KRG19-B04)

The Kurobegawa granodiorite is a granitic intrusive body exposed in the northern Hida mountain range in central Honshu Island, Japan (Fig. 1c). Zircon U–Pb ages indicate that it is the youngest plutonic rock presently exposed on the surface of the Earth (ca. 0.8 Ma; Ito et al., 2013, 2017; Suzuki et al., 2022). This granodiorite is characterized by numerous mafic magmatic enclaves and is subdivided into three units – lower, middle, and upper – based on the areal proportion of mafic magmatic enclaves in an outcrop (Harayama et al., 2000). Monazite in KRG19-B04 was separated from the biotite–hornblende granite in the lower unit. Monazite in KRG19-B04 shows a semi-euhedral or anhedral shape and is commonly colorless (Fig. 2c). It encloses mineral inclusions of quartz, biotite, and pyrite; a primary polyphase mineral inclusion; and secondary fluid inclusions. Secondary domains that cut the primary sector-zoned domain are commonly observed in BSE images (Fig. 2d).

2.3 The Muro ignimbrite (MR3b)

The Muro ignimbrite is a siliciclastic eruptive rock widely distributed in the northern part of the Kii Peninsula, Hon-

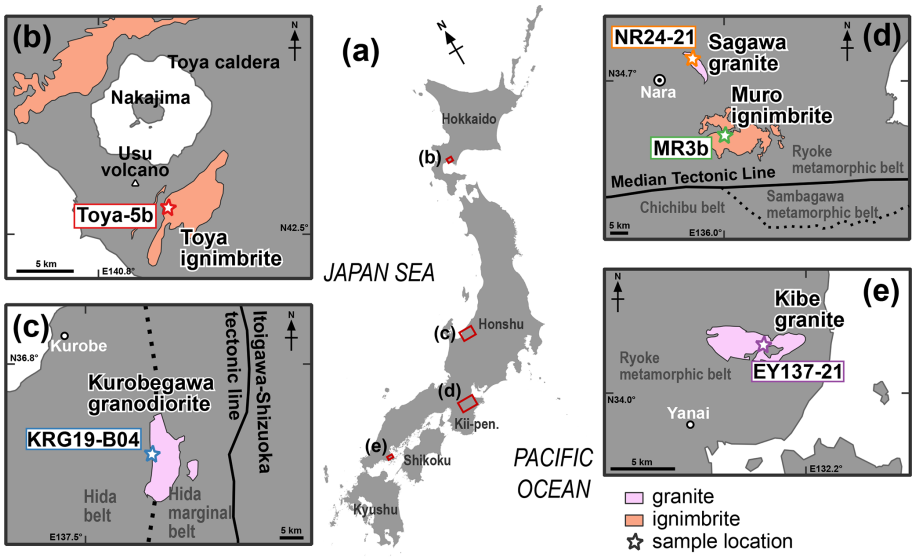

Figure 1. Geological units from which rock samples were collected as part of this study along with a map of the sampling sites. **(a)** Index map. **(b)** The Toya ignimbrite is distributed around the Toya caldera in the western part of Hokkaido. **(c)** The Kurobegawa granodiorite is exposed in the Hida Mountains in the central part of the island of Honshu. **(d)** The Sagawa granite and the Muro ignimbrite are distributed in the northern part of the Kii Peninsula, located on Honshu Island. **(e)** The Kibe granite is exposed in the southwestern part of the island of Honshu.

shu Island (Fig. 1d). The zircon and apatite FT ages obtained from the black glassy lapilli tuff at the base of the unit indicate that the Muro ignimbrite originated from an extensive igneous activity take took place at ca. 15 Ma (Iwano et al., 2007, 2009). The monazite sample employed in this study was separated from the siliceous ignimbrite (MR3b) overlying the black glassy lapilli tuff, which crops out at the same location as MR3 (Iwano et al., 2007). Monazite in MR3b is yellowish and euhedral (Fig. 2e). It includes numerous polyphase inclusions composed of quartz, K-feldspar, and magnetite. BSE images show no zoning or very weak oscillatory zoning.

2.4 The Kibe granite (EY137-21)

The Kibe granite is a porphyritic granite body from the Ryoke belt and is exposed in the Yanai area in southeastern Honshu Island (Fig. 1e). The middle Cretaceous zircon U–Pb dates (98.0 ± 1.0 and 97.6 ± 1.0 Ma (2σ)) have been interpreted as intrusive ages for this pluton (Skrzypek et al., 2016). Jones et al. (2023) reported Late Cretaceous to Paleocene zircon and apatite (U–Th)/He and apatite FT dates. They also conducted MFT dating and calculated a central age of 2.2 ± 0.1 Ma (1σ) using the absolute calibration method (Hasebe et al., 2004), including undetermined parameters (e.g., the assumption that the initial FT length is 10.6 µm; Jones et al., 2021). The monazite sample used in this study was separated from the biotite granite (EY137-21) collected from the riverbed 100 m east of EY137A, as used in Skrzypek et al. (2016) and Jones et al. (2023). Monazite in EY137-21 is a yellow- or orange-colored semi-euhedral crystal (Fig. 2g). Fine inclusions of quartz, biotite, apatite, and zircon are commonly found. Internal structures of oscillatory zoning and/or sector zoning are commonly observed in BSE images (Fig. 2h). Secondary domains that cut the primary microstructures are found in some grains.

2.5 The Sagawa granite (NR24-21)

The Sagawa granite is a Cretaceous granitic body from the Ryoke belt and is exposed in the northern part of the Kii Peninsula on the island of Honshu (Fig. 1d). The exact intrusion age is unknown, although a middle Cretaceous biotite Rb–Sr age (> 106 Ma) was reported by Ishizuka et al. (1996). Similar to the Kibe granite, Jones et al. (2023) reported Late Cretaceous to Eocene zircon and apatite (U–Th)/He and apatite FT dates, and they noted an MFT central age of 1.7 ± 0.1 Ma (1σ). The monazite sample used in this study was separated from the biotite granite (NR24-21) collected from the same outcrop of NR24B as that used in Jones et al. (2023). Monazite in NR24-21 is a yellow- or orange-colored semi-euhedral crystal (Fig. 2i) with minor mineral inclusions of quartz, biotite, apatite, and zircon. Oscillatory zoning and/or sector zoning are commonly observed in BSE images (Fig. 2j). Secondary domains that cut the primary microstructure are found in some grains.

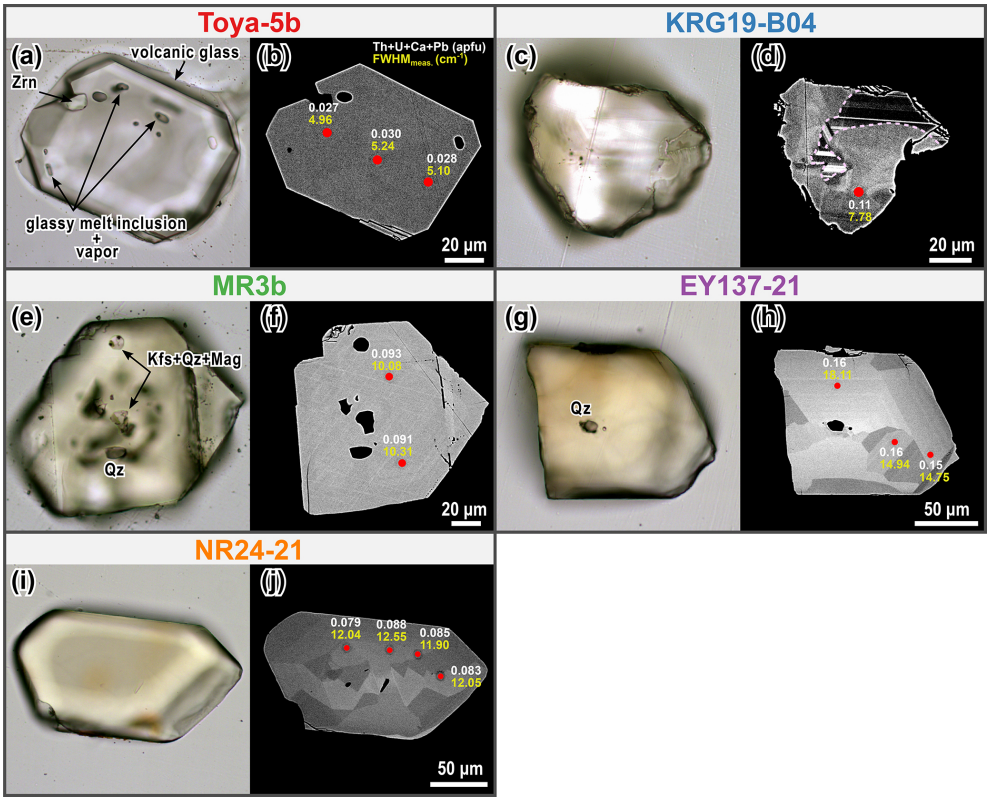

Figure 2. Photomicrographs and BSE images of representative monazite grains. **(a, b)** A colorless euhedral monazite from Toya-5b originating from the Toya ignimbrite. Glassy melt inclusions and zircon (Zrn) often appear as inclusions. BSE image shows the homogeneity of the intra-grain composition. $FWHM_{meas.}$ denotes the measured Raman band broadening. **(c, d)** A colorless and anhedral monazite from KRG19-B04 originating from the Kurobegawa granodiorite. The dashed line indicates the boundary between primary and secondary domains observed in the BSE image. **(e, f)** A yellow-colored euhedral monazite from MR3b originating from the Muro ignimbrite. This monazite contains mineral inclusions of quartz and zircon, as well as polyphase solid inclusions composed of quartz (Qz), K-feldspar (Kfs), and magnetite (Mag). A BSE image shows the compositional homogeneity within the grain. **(g, h)** A yellow-colored semi-euhedral monazite from EY137-21 originating from the Kibe granite. Internal structures of oscillatory zoning and/or sector zoning are observed in the BSE image. **(i, j)** A yellow-colored semi-euhedral monazite from NR24-21 originating from the Sagawa granite. Internal structures of sector zoning are observed in the BSE image. Mineral abbreviations follow those given by Warr (2021).

3 Method

3.1 Estimation of the structural disorder and chemical composition

The degree of accumulated radiation damage in monazite was estimated using Raman spectroscopic measurements. The Raman band broadening (full width at half maximum (FWHM); cm^{-1}) of the $\upsilon_1(PO_4)$ peak is widely applied as an index for structural disorder (Seydoux-Guillaume et al., 2002; Ruschel et al., 2012). On the other hand, Raman band broadening depends not only on self-irradiation but also on the incorporation of non-formula elements into monazite. Therefore, the degree of accumulated radiation damage (Δ_{FWHM}) is estimated as the difference between the measured Raman band broadening ($FWHM_{meas.}$) and the chemical band broadening ($FWHM_{calc.}$) and is expressed as

$$\Delta_{FWHM} = FWHM_{meas.} - FWHM_{calc.} \quad (1)$$

$FWHM_{calc.}$ is calculated using the calibration by Ruschel et al. (2012):

$$FWHM_{calc.} = 3.95 + 26.66 \times (Th + U + Ca + Pb)\,[apfu]. \quad (2)$$

To avoid any possible effects of the focused electron beam on accumulated radiation damage, Raman spectroscopic measurements were carried out prior to conducting electron probe microanalyses (Meldrum et al., 1996). Since the measurement points were selected before the BSE image observation, 50 points for each sample were selected to avoid inclusions and cracks, regardless of the internal structure.

3.1.1 Sample preparation

Mineral separation was conducted at the Tono Geoscience Center and Kyoto Fission-Track Co., Ltd. Rock samples were crushed using a stainless-steel mortar. For Toya-5b, white pumice (Goto et al., 2018) was picked out from the

unit 5b pumice bed, washed, dried, and crushed. Monazite grains were separated using standard heavy-liquid-separation and magnetic-separation techniques. They were handpicked and oriented parallel to the (100) pinacoid faces on a Teflon block. They were then mounted on epoxy resin (Konishi E205) at room temperature and polished using a grinding plate with diamond pastes of 3 and 1 µm diameter.

3.1.2 Raman spectroscopic measurements

The Raman spectrum of monazite samples was measured using a laser Raman spectrometer (JASCO NRS 3100) at Kyoto University at room temperature (ca. 21 °C). A green YAG laser (532 nm) was irradiated at the polished monazite surface through a filter with an optical density of 1, a 0.05 mm slit, and a 100× objective lens. A grating with 1800 grooves mm^{-1} was used to disperse the light to be analyzed, resulting in a spectral resolution of 1 cm^{-1}. The laser power at the sample surface was ∼ 3.0 mW. The spectrum covered the wavenumber interval of 200–1400 cm^{-1} and was recorded in four acquisitions of 10 s. Raman shift was calibrated using the 520.7 cm^{-1} band of a Si wafer and a built-in Ne lamp. The spectrometer drift was assessed by measuring the Ne lamp emissions every 10 unknown measurements. The accuracy of the wavenumber was better than 0.5 cm^{-1}.

Measured Raman spectra were cropped between 800–1200 cm^{-1}, including the $v_1(PO_4)$ band, and corrected for fluorescence background by subtracting a linear baseline. The spectra were fitted using a Lorentzian–Gaussian (pseudo-Voigt) function to determine the peak position and width. Peak fitting was conducted using PeakFit v4.12 (SYSTAT) software. An artificial broadening of the signal was corrected mathematically using the empirical correction method from Váczi (2014).

3.1.3 Electron probe microanalysis

In situ chemical analyses were conducted at the same spot as the Raman spectroscopic measurements using a JXA-8530F field-emission electron probe microanalyzer (JEOL, Ltd.) at the Tono Geoscience Center. Spot analyses were operated at an accelerating voltage of 15 kV, a beam current of 20 nA, and a beam diameter of 5 µm. The background counting times were set at half of the respective peak counting times. Natural and synthetic minerals (Astimex REEM25–15 and MINM25–53) were used as standards, and ZAF correction was applied. The counting times were set at 30 s for rare-earth elements (REEs), Ca, P, and Y; 60 s for Th and U; and 15 s for Pb and Si. For the measurement of UO_2 (UMβ), a peak interference correction by ThO_2 (ThMγ) was applied.

3.2 Etching of monazite fission tracks

MFTs can be etched with HCl (Shukoljukov and Komarov, 1970; Weise et al., 2009; Jones et al., 2019). In this study, we adopted the etching protocol proposed by Jones et al. (2019) – 6 M HCl at 90 °C for 60–90 min, with temperature control facilitated by a water bath. Despite the adherence to specified conditions, some samples exhibited insufficient etching even after 90 min, necessitating additional step-etching procedures.

For step-etching procedures, the etching termination criterion needed to be carefully determined for reliable analysis. Theoretically, etching can be performed until the entire track length is etched and as long as the measured FT density does not change. However, as it is difficult to determine this in practice, the width of the FT has been adopted as an etching index for zircon over the past few decades (e.g., Hasebe et al., 1994; Yamada et al., 1995). Also, previous etching experiments with respect to monazite have indicated that the etch pit diameter parallel to the crystallographic *c* axes (Dpc) upon completion of the etching is approximately 0.8 µm (Jones et al., 2022). While the termination conditions for FT dating require more careful consideration, for the sake of convenience, this study adopted a Dpc length of 0.8 µm as the termination criterion and employed a stepwise etching procedure to estimate the total etching duration (t_{MFT}).

4 Results

For each sample in this study, 50 Raman spectra and corresponding chemical compositions were obtained at the same spot. Representative values are shown in Table 2, and data for each spot are summarized in Tables S1–S10 in the Supplement. The $FWHM_{meas.}$ values and non-formula element composition (Th + U + Ca + Pb) for each spot are shown in Fig. 3a, and violin plots illustrating Δ_{FWHM} calculated from them are shown in Fig. 3b. The following sections summarize the results of the Raman spectroscopic analysis, electron probe microanalysis, calculated degree of radiation damage, and MFT etching experiment.

4.1 Raman spectroscopic measurements

The $FWHM_{meas.}$ value measured using Raman spectroscopy was significantly smaller for monazites from Toya-5b and KRG19-B04, i.e., from the younger samples, with mean values of 4.98 and 6.92 cm^{-1}, respectively. The $FWHM_{meas.}$ value of MR3b (10.44 cm^{-1}) was larger than those of the younger samples and tended to be smaller than those of the Cretaceous granites (14.47 and 12.61 cm^{-1} for EY137-21 and NR24-21, respectively). Toya-5b showed very low dispersion, whereas the other four samples showed relatively high dispersion for each measurement spot.

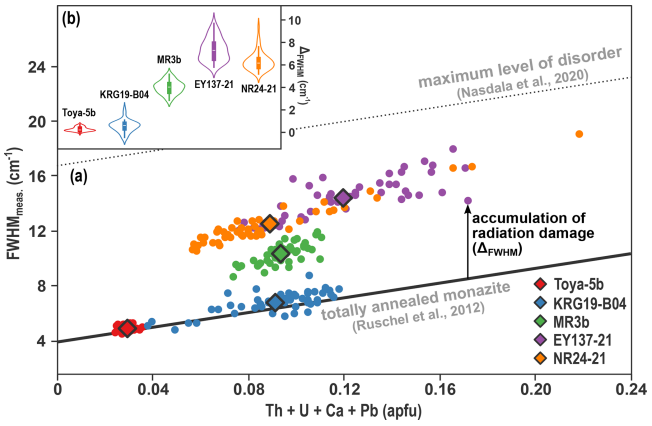

Figure 3. **(a)** Correlation of $FWHM_{meas.}$ with the sum of Th, U, Ca, and Pb (apfu) for five natural monazite samples. Points indicate individual measurements, and diamonds indicate the average values for the different samples. The solid line in the figure shows the calibration of the chemical broadening ($FWHM_{calc.}$) from Ruschel et al. (2012). The data shift along the vertical axis as structural disorder increases due to radiation damage. The structural disorder of monazite is partially recovered by self-irradiation, meaning that structural disorder no longer progresses beyond a certain level (dashed line), and natural monazite does not undergo metamictization (Nasdala et al., 2020). **(b)** Violin plots combined with box plots of Δ_{FWHM}.

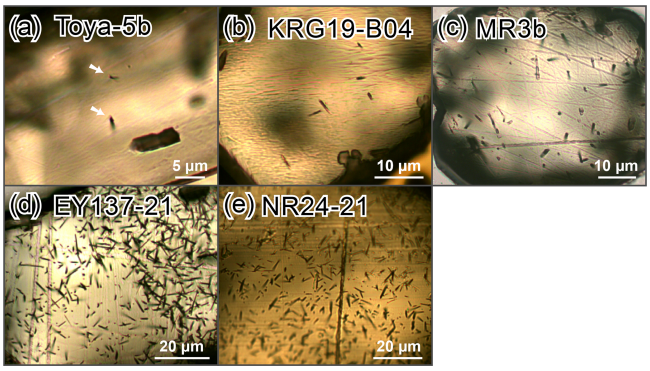

Figure 4. Photomicrographs of etched MFTs in **(a)** Toya-5b, **(b)** KRG19-B04, **(c)** MR3b, **(d)** EY137-21, and **(e)** NR24-21.

4.2 Chemical composition of the natural monazite sample

All five monazites were classified as monazite-(Ce) and showed no significant dispersion in ratios of light rare-earth elements (LREEs) (La–Ce–Nd–Pr; Tables S1–S5). Monazite in Toya-5b tended to have a very homogeneous inter- and intra-grain composition and was poor in non-formula elements (Fig. 3a). While monazite in MR3b was very homogeneous within each grain, significant variation in inter-grain chemical composition was observed. As seen in the BSE images, KRG19-B04, EY137-21, and NR24-21 were diverse in inter- and intra-grain composition. Regarding Th, U, Ca, and Pb concentrations, although variations existed from point to point, these elements tended to be enriched on average in the following sequence: Toya-5b < NR24-21 < KRG19-B04 < MR3b < EY137-21.

4.3 The degree of radiation damage

The degree of radiation damage (Δ_{FWHM}) estimated for the monazites in each sample is based on Eq. (1) and shown in Table 2 and Fig. 3b. The mean Δ_{FWHM} values are arranged in ascending order as follows: 0.27 cm^{-1} for Toya-5b, 0.55 cm^{-1} for KRG19-B04, 4.01 cm^{-1} for MR3b, 6.31 cm^{-1} for NR24-21, and 7.35 cm^{-1} for EY137-21. This relationship is roughly consistent with that of sample ages (Table 1). These values suggest a progressive increase in structural disorder among the samples caused by the accumulation of radiation damage. A high dispersion within the sample was observed in four samples (KRG19-B04, MR3b, EY137-21, and NR24-21), indicating variations in chemical composition. Toya-5b exhibited very low dispersion with respect to radiation damage, reflecting a very homogeneous inter- and intra-grain chemical composition. Although some spots had negative Δ_{FWHM} values for monazites in Toya-5b and KRG19-B04, we considered these to be attributed to measurement uncertainty and error propagation in the calibration of chemical broadening given by Ruschel et al. (2012) (Eq. 2). Thus, we did not reject these negative values.

4.4 Chemical etching of monazite fission tracks

All five monazite samples underwent MFT etching procedures following the conditions outlined by Jones et al. (2019) – 60–90 min in 6 M HCl at 90 °C. However, only MFTs of monazites in EY137-21 (Fig. 4d) achieved a Dpc length of 0.8 µm within 90 min. Monazites in MR3b and NR24-21 exhibited under-etched MFTs, while monazites in Toya-5b and KRB19-B04 exhibited no observable MFTs. Subsequently, additional step-etching procedures (40–120 min) were employed for these four samples. Most Dpc lengths reached 0.8 µm at 120 min for NR24-21 (Fig. 4e) and at 210 min for MR3b (Fig. 4c). For Toya-5b and KRB19-B04, several FTs appeared approximately at 500 min, and the etching was finally completed at 1200 min for Toya-5b (Fig. 4a) and at 860 min for KRB19-B04 (Fig. 4b). It should be noted that for Toya-5b and KRB19-B04, the timing at which the Dpc length reached 0.8 µm for each FT varied significantly from grain to grain, with each having an error of about ±120 min. For both NR24-21 and EY137-21, intra-grain heterogeneity in track density was observed. In these samples, the FT etching rate tended to be faster in the domains with a higher FT density (Fig. 4d). Most grains in Toya-5b were zero-track, and nine MFTs were observed in 61 grains.

Table 1. Coordinates and lithology of rock samples used in this study.

Sample name	Lat (degrees N)	Long (degrees E)	Unit name	Rock type	Reference age*
Toya-5b	42.5276	140.8786	Toya ignimbrite (unit 5b; Goto et al., 2018)	pyroclastic-flow deposit (monazites are mainly obtained from white pumice)	$113.5^{+5.4}_{-5.2}$ ka (Zrn and Mnz U–Th; Niki et al., 2022) ca. 108 ka (Zrn U–Th; Ito et al., 2014)
KRG19-B04	36.6430	137.6860	Kurobegawa granodiorite (lower unit; Harayama et al., 2000)	biotite–hornblende granodiorite	ca. 0.8 Ma (ZUPb; Ito et al., 2013; Suzuki et al., 2022) < 1 Ma (ZFT and ZHe; Yamada, 1999; King et al., 2022)
MR3b	34.5565	136.0411	Muro ignimbrite	felsic ignimbrite	ca. 15 Ma (AFT; Iwano et al., 2009) 15.2 ± 0.5 Ma (ZFT; Iwano et al., 2007)
EY137-21	34.0287	132.1632	Kibe granite	biotite granite	ca. 98 Ma (ZUPb; Skrzypek et al., 2016) 72.3–68.2 Ma (ZHe; Jones et al., 2023) 60.3 ± 1.5 Ma (AFT; Jones et al., 2023) 72.5–70.0 Ma (AHe; Jones et al., 2023) 2.2 ± 0.1 Ma (MFT; Jones et al., 2023)
NR24-21	34.7224	135.9414	Sagawa granite	biotite granite	ca. 116–106 Ma (Bt Rb–Sr; Ishizaka, 1966) 75.8–37.3 Ma (ZHe; Jones et al., 2023) 53.4 ± 1.2 Ma (AFT; Jones et al., 2023) 83.4–41.0 Ma (AHe; Jones et al., 2023) 1.7 ± 0.1 Ma (MFT; Jones et al., 2023)

* Ages reported from the same location or stratigraphic unit are given with errors (95 % confidence levels or 1σ), whereas ages reported from the same geological unit are given as approximate age values. Zrn: zircon. Mnz: monazite. ZUPb: zircon U–Pb date. ZFT: zircon fission-track date. ZHe: zircon (U–Th)/He date. AFT: apatite fission-track date. AHe: apatite (U–Th–Sm)/He date. MFT: monazite fission-track date. BT: biotite.

5 Discussion

5.1 Inverse correlation between radiation damage and fission-track etching time on monazite

The degree of radiation damage (Δ_{FWHM}) generally exhibits a positive correlation with sample age, except for EY137-21 (ca. 98 Ma) and NR24-21 (> 105 Ma). Jones et al. (2023) reported younger cooling ages (zircon and apatite (U–Th)/He ages and apatite and monazite FT ages) for NR24-21 than for EY137-21. Notably, radiation damage in monazite can undergo thermal annealing, similar to MFTs (Seydoux-Guillaume et al., 2002), suggesting that Δ_{FWHM} may positively correlate not with crystallization age but with the timing of cooling at a specific temperature. As mentioned above, the order of t_{MFT} is as follows: Toya-5b > KRG19-B04 > MR3b > NR24-21 > EY137-21. This demonstrates an inverse correlation with Δ_{FWHM}. As shown in Fig. 5, these parameters exhibit an obvious inverse proportion.

This correlation mirrors the inverse relationship observed for the etching time of zircon FTs and spontaneous FT density (Krishnaswami et al., 1974; Gleadow et al., 1976). Previous studies have considered FT density as a proxy for U concentration, positing that zircon with a higher degree of radiation damage exhibits a more rapid FT etching rate. The accelerated etching rate along the FT, relative to the etching

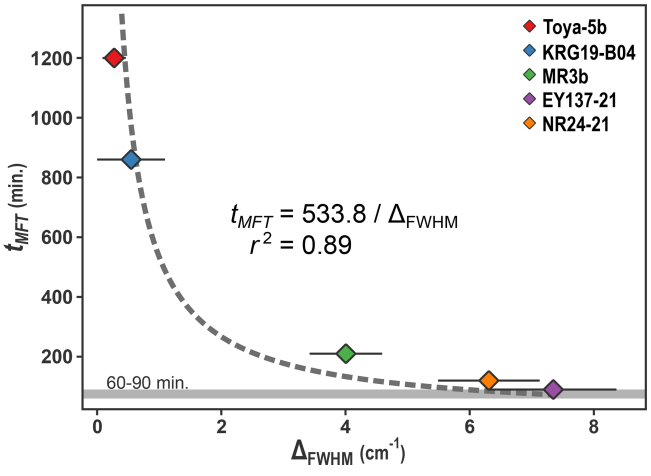

Figure 5. Correlation of t_{MFT} with Δ_{FWHM} for five natural monazite samples. The dashed line denotes the fitted inversely proportional equation using the least-squares method, with the equation and r^2 score shown in the center of the figure. The gray band at the bottom of the diagram represents the etching time indicated in previous studies (Jones et al., 2019).

rate of the bulk crystals, primarily accounts for the FT etching time required for etching bulk crystals. The inverse correlation between FT etching time and spontaneous FT density is interpreted as a reflection of the diminished chemical resistance of bulk zircon crystals resulting from radiation damage.

The inverse correlation between t_{MFT} and Δ_{FWHM} revealed in this study can be explained by the same function as that observed in zircon FT. Similar to zircon, etching along MFTs is assumed to proceed rapidly following immersion in HCl (5–15 min; Jones et al., 2022). Consequently, the MFT etching time is predominantly regarded as the duration necessary for the bulk etching of the monazite crystals. It is reasonable to explain this phenomenon by suggesting that the etching time has been shortened in response to the diminished chemical resistance of bulk crystals, a consequence of monazite self-irradiation.

Meanwhile, the correlation between the chemical composition of monazite and t_{MFT} is unclear based on the results of this study because the monazite samples have a similar chemical composition. As it is a phosphate mineral, monazite generally exhibits considerable variability in solid-solution compositions (Ce–La–Nd–Pr) and trace-element compositions. This variability may result in differences in etching rates depending on the composition, similar to apatite (e.g., Burtner et al., 1994; Ravenhurst et al., 2003). Despite the absence of significant differences in solid-solution compositions, particularly regarding the average content of non-formula cations (Th, U, Ca, and Pb), between KRG19-B04, MR3b, and NR24-21, there were notable differences in t_{MFT} among the monazites in this study. In these samples, the variation in t_{MFT} primarily signifies the influence of radiation damage rather than that of chemical composition. A similar investigation using monazite samples exhibiting a range of solid-solution compositions is required to clarify the specific impact of chemical composition on t_{MFT}. It remains challenging to ascertain whether the dominant factor is chemical composition or radiation damage. Nevertheless, the results of this study strongly indicate that radiation damage significantly influences MFT etching time.

5.2 Etching of young and ordered monazite

In the present study, MFTs in samples other than EY137-21 exhibited under-etching when subjected to the etching protocol outlined in the previous study (6 M HCl, 90 °C, 60–90 min; Jones et al., 2019). This outcome can be attributed to the comparatively lower radiation damage levels in the samples employed here compared to those utilized in previous studies. Monazites from previous studies, such as the Antsirabe monazite (ca. 500 Ma) and the Harcourt monazite (ca. 370 Ma), are older than the monazites examined in this study and are presumed to exhibit more advanced radiation damage (Weise et al., 2009; Jones et al., 2019). While earlier investigations have confirmed the complete annealing of MFTs through pre-annealing, the conditions employed (at

Table 2. Representative results of Raman and electron probe microanalyses, calculated Δ_{FWHM} values, and t_{MFT} for monazites in five rock samples.

Sample name		Electron probe microanalysis (weight %)																		Raman analysis (cm^{-1})		Δ_{FWHM} (cm^{-1})	t_{MFT} (min)
		SiO_2	P_2O_5	CaO	Y_2O_3	ThO_2	UO_2	PbO	La_2O_3	Ce_2O_3	Pr_2O_3	Nd_2O_3	Sm_2O_3	Eu_2O_3	Gd_2O_3	Tb_2O_3	Dy_2O_3	Ho_2O_3	Er_2O_3	Tm_2O_3	Yb_2O_3	Total	Th+U+Ca+Pb (apfu)	Shift ($\nu_1(PO_4)$)	$FWHM_{meas.}$ ($\nu_1(PO_4)$)		
Toya-5b	spot 33	0.40	28.98	0.23	1.57	2.15	0.01	n.d.	11.31	30.38	2.95	14.26	2.14	n.d.	4.24	n.d.	0.53	0.77	n.d.	n.d.	n.d.	99.90	0.029	972.61	5.32	0.39	1200
KRG19-B04	spot 20	1.30	27.29	0.42	2.09	7.52	0.10	n.d.	11.67	30.02	2.65	9.98	1.41	n.d.	3.75	n.d.	0.52	0.49	0.01	n.d.	n.d.	99.19	0.088	973.41	6.90	0.61	860
MR3b	spot 38	0.28	29.69	0.98	3.10	5.60	0.04	n.d.	9.60	28.47	2.64	11.34	2.13	n.d.	4.29	n.d.	0.88	0.81	n.d.	0.01	n.d.	99.86	0.091	972.76	10.71	4.32	210
EY137-21	spot 06	1.44	27.73	0.58	1.90	8.29	0.17	n.d.	10.78	29.31	2.66	10.32	1.73	n.d.	3.88	n.d.	0.55	0.56	0.02	n.d.	n.d.	99.92	0.102	971.43	13.14	6.49	90
NR24-21	spot 18	0.85	28.63	0.71	2.41	5.52	0.19	n.d.	11.80	30.20	2.59	9.76	1.50	n.d.	3.80	n.d.	0.60	0.47	0.01	n.d.	n.d.	99.04	0.088	971.55	12.43	6.30	120

400 °C for 24 h (Weise et al., 2009) and 18 h (Jones et al., 2019)) are inadequate for achieving the total annealing of radiation damage (which requires 10 d at 900 °C; Seydoux-Guillaume et al., 2002). Consequently, it is presumed that a certain degree of radiation damage persists in these samples. Moreover, the structural disorder of monazite is partially recovered by self-irradiation, meaning that structural disorder no longer progresses beyond a certain level (ca. 12 cm^{-1} in Δ_{FWHM}), and natural monazite does not undergo metamictization (Nasdala et al., 2020). As a result, structural disorder in monazites older than a certain age tends to concentrate at a specific degree of radiation damage. For such samples, MFT etching is considered feasible within 60–90 min, as proposed in previous studies.

On the contrary, younger monazites with lower levels of radiation damage exhibit high chemical resistance, and existing etching protocols fail to adequately etch MFTs. Fitting the t_{MFT} and Δ_{FWHM} data with an inverse proportional function using the least-squares method yields a r^2 value of 0.89 (Fig. 5: $t_{MFT} = 533.84$ per Δ_{FWHM}). This equation indicates a rapid increase in t_{MFT}, particularly in minimally damaged monazite, as Δ_{FWHM} decreases below 2 cm^{-1}. Even Miocene eruptive rocks require more than double the standard etching time (210 min for MR3b), indicating that current etching protocols may prove insufficient for Cenozoic geological samples. Furthermore, radiation damage in monazite undergoes thermal annealing. This implies that even if the crystallization age of monazite is sufficiently old, similar challenges with respect to etching may arise if the sample experienced medium- to high-temperature conditions during the Cenozoic.

When applying the MFT method to rock samples with more recent formation and cooling ages in active tectonic settings, it is necessary to develop protocols that effectively etch chemical-resistant monazite. In the case of zircon, which is characterized by a similar diversity in etching times as monazite, previous studies have defined the etching termination criteria and implemented a step-etching method to meet these criteria (e.g., Yamada et al., 1993, 1995). As the application of MFT dating expands, it is recommended to investigate termination criteria that are specific to MFT etching and adopt a step-etching approach.

6 Conclusions

In this study, we conducted measurements of Raman spectra and chemical composition of monazite samples ranging from the Cretaceous to the Quaternary and compared the results with MFT etching experiment. The results reveal an inverse proportion between MFT etching time and the degree of radiation damage in monazite, while the correlation between MFT etching time and chemical composition remains unclear. The results of the present study confirm previous considerations that the etching rate of MFTs is predominantly influenced by radiation damage. On the other hand, young samples with lower levels of radiation damage exhibit higher chemical resistance, indicating that existing etching recipes may not sufficiently etch MFTs. Future applications of MFT dating for younger geological samples will necessitate the determination of termination criteria for MFT etching and the adoption of step-etching procedures.

Data availability. All data used in this study can be found in the Supplement.

Supplement. The supplement related to this article is available online at: https://doi.org/10.5194/gchron-6-313-2024-supplement.

Author contributions. Rock samples were collected by TN, SF, SS, and SN. Mineral separation was conducted by TN and TD. Raman spectroscopic measurements and data analysis were conducted by TN and TK. Electron probe microanalysis was carried out by TN. The MFT etching experiment was conducted by SF and TN. This study was conceptualized by TT and TD.

Competing interests. At least one of the (co-)authors is a member of the editorial board of *Geochronology*. The peer-review process was guided by an independent editor, and the authors also have no other competing interests to declare.

Disclaimer. Publisher's note: Copernicus Publications remains neutral with regard to jurisdictional claims made in the text, published maps, institutional affiliations, or any other geographical representation in this paper. While Copernicus Publications makes every effort to include appropriate place names, the final responsibility lies with the authors.

Acknowledgements. We would like to thank Birk Härtel and Sean Jones for their constructive comments, which greatly improved the paper. We also thank Hideki Iwano (Kyoto Fission-Track Co., Ltd.) and Etienne Skrzypek (University of Graz) for providing important information on monazite samples. Raman spectroscopic measurements were carried out with the assistance of Fumiko Higashino (Kyoto University).

Financial support. This study was funded by the Ministry of Economy, Trade and Industry, Japan, as part of its R&D supporting program titled "Establishment of Technology for Comprehensive Evaluation of the Long-term Geosphere Stability on Geological Disposal Project of Radioactive Waste" (grant no. JPJ007597; fiscal year 2023).

Review statement. This paper was edited by Norbert Frank and reviewed by Sean Jones and Birk Härtel.

References

Burtner, R. L., Nigrini, A., and Donelick, R. A.: Thermochronology of Lower Cretaceous Source Rocks in the Idaho-Wyoming Thrust Belt, Am. Assoc. Pet. Geol. Bull., 78, 1613–1636, https://doi.org/10.1306/A25FF233-171B-11D7-8645000102C1865D, 1994.

Fayon, A. K.: Fission Track Dating of Monazite: Etching Efficiencies as a Function of U Content, in: GSA Annual Meeting, Geological Society of America, Minneapolis, p. 331, 2011.

Fleischer, R. L. and Price, P. B.: Techniques for geological dating of minerals by chemical etching of fission fragment tracks, Geochim. Cosmochim. Ac., 28, 1705–1714, https://doi.org/10.1016/0016-7037(64)90017-1, 1964.

Gleadow, A. J. W., Hurford, A. J., and Quaife, R. D.: Fission track dating of zircon: Improved etching techniques, Earth Planet. Sc. Lett., 33, 273–276, https://doi.org/10.1016/0012-821X(76)90235-1, 1976.

Goto, Y., Suzuki, I, K., Shinya, T., Yamauchi, I., A., Miyoshi, M., Danhara, T., and Tomiya, A.: Stratigraphy and Lithofacies of the Toya Ignimbrite in Southwestern Hokkaido, Japan: Insights into the Caldera-forming Eruption at Toya Caldera, J. Geogr. (Chigaku Zasshi), 127, 191–227, https://doi.org/10.5026/jgeography.127.191, 2018.

Green, P. F.: The relationship between track shortening and fission track age reduction in apatite: combined influences of inherent instability, annealing anisotropy, length bias and system calibration, Earth Planet. Sc. Lett., 89, 335–352, https://doi.org/10.1016/0012-821X(88)90121-5, 1988.

Harayama, S., Takahashi, Y., Nakano, S., Kariya, Y., and Komazawa, M.: Geology of the Tateyama District, Geol. Surv. of Jpn., Tsukuba, 218 pp., 2000.

Hasebe, N., Tagami, T., and Nishimura, S.: Towards zircon fission-track thermochronology: Reference framework for confined track length measurements, Chem. Geol., 112, 169–178, https://doi.org/10.1016/0009-2541(94)90112-0, 1994.

Hasebe, N., Barbarand, J., Jarvis, K., Carter, A., and Hurford, A. J.: Apatite fission-track chronometry using laser ablation ICP-MS, Chem. Geol., 207, 135–145, https://doi.org/10.1016/j.chemgeo.2004.01.007, 2004.

Ishizaka, K.: A geochronological study of the Ryoke metamorphic terrain in the Kinki district, Japan, in: Memoirs Coll. Sci. Univ. Kyoto, 69–102, https://doi.org/10.14989/doctor.k532, 1966.

Ito, H., Yamada, R., Tamura, A., Arai, S., Horie, K., and Hokada, T.: Earth's youngest exposed granite and its tectonic implications: The 10–0.8 Ma Kurobegawa Granite, Sci. Rep., 3, 1–5, https://doi.org/10.1038/srep01306, 2013.

Ito, H.: Zircon U-Th-Pb dating using LA-ICP-MS: Simultaneous U-Pb and U-Th dating on the 0.1 Ma Toya Tephra, Japan, J. Volcanol. Geotherm. Res., 289, 210–223, https://doi.org/10.1016/j.jvolgeores.2014.11.002, 2014.

Ito, H., Spencer, C. J., Danišík, M., and Hoiland, C. W.: Magmatic tempo of Earth's youngest exposed plutons as revealed by detrital zircon U-Pb geochronology, Sci. Rep., 7, 4–9, https://doi.org/10.1038/s41598-017-12790-w, 2017.

Iwano, H., Danhara, T., Hoshi, H., Kawakami, Y., Sumii, T., Shinjoe, H., and Wada, Y.: Simultaneity and similarity of the Muro Pyroclastic Flow Deposit and the Kumano Acidic Rocks in Kii Peninsula, southwest Japan, based on fission track ages and morphological characteristics of zircon, J. Geol. Soc. Jpn., 113, 326–339, https://doi.org/10.5575/geosoc.113.326, 2007.

Iwano, H., Danhara, T., and Hoshi, H.: Fission track ages on apatite from Miocene igneous rocks in the Kii Peninsula, Japan, J. Geol. Soc. Jpn., 115, 427–432, https://doi.org/10.5575/geosoc.115.427, 2009.

Jones, S., Gleadow, A., Kohn, B., and Reddy, S. M.: Etching of fission tracks in monazite: An experimental study, Terra Nova, 2018, 179–188, https://doi.org/10.1111/ter.12382, 2019.

Jones, S., Gleadow, A., and Kohn, B.: Thermal annealing of implanted ^{252}Cf fission tracks in monazite, Geochronology, 3, 89–102, https://doi.org/10.5194/gchron-3-89-2021, 2021.

Jones, S., Kohn, B., and Gleadow, A.: Etching of fission tracks in monazite: Further evidence from optical and focused ion beam scanning electron microscopy, Am. Mineral., 107, 1065–1073, https://doi.org/10.2138/am-2022-8002, 2022.

Jones, S., Kohn, B., Gleadow, A., Skrzypek, E., and Tagami, T.: Low-temperature thermochronology of Ryoke belt granitoids, SW Japan: New insights into the recent cooling history from monazite fission-track dating, Tectonophysics, 864, 229998, https://doi.org/10.1016/j.tecto.2023.229998, 2023.

Ketcham, R. A., Carter, A., and Hurford, A. J.: Inter-laboratory comparison of fission track confined length and etch figure measurements in apatite, Am. Mineral., 100, 1452–1468, https://doi.org/10.2138/am-2015-5167, 2015.

King, G. E., Ahadi, F., Sueoka, S., Herman, F., Anderson, L., Gautheron, C., Tsukamoto, S., Stalder, N., Biswas, R., Fox, M., Delpech, G., Schwartz, S., and Tagami, T.: Eustatic change modulates exhumation in the Japanese Alps, Geology, 51, 131–135, https://doi.org/10.1130/G50599.1, 2022.

Krishnaswami, S., Lal, D., Prabhu, N., and Macdougall, D.: Characteristics of fission tracks in zircon: Applications to Geochronology and Cosmology, Earth Planet. Sc. Lett., 22, 51–59, https://doi.org/10.1016/0012-821X(74)90063-6, 1974.

Laslett, G. M., Kendall, W. S., Gleadow, A. J. W., and Duddy, I. R.: Bias in measurement of fission-track length distributions, Nucl. Tracks Radiat. Meas., 6, 79–85, https://doi.org/10.1016/0735-245X(82)90031-X, 1982.

Laslett, G. M., Gleadow, A. J. W., and Duddy, I. R.: The relationship between fission track length and track density in apatite, Nucl. Tracks Radiat. Meas., 9, 29–38, https://doi.org/10.1016/0735-245X(84)90019-X, 1984.

Meldrum, A., Wang, L. M., and Ewing, R. C.: Ion beam induced amorphization of monazite, Nucl. Instrum. Meth. B, 116, 220–224, https://doi.org/10.1016/0168-583X(96)00037-7, 1996.

Nasdala, L., Akhmadaliev, S., Burakov, B. E., and N, C. C.: The absence of metamictisation in natural monazite, Sci. Rep., 10, 14676, https://doi.org/10.1038/s41598-020-71451-7, 2020.

Niki, S., Kosugi, S., Iwano, H., Danhara, T., and Hirata, T.: Development of an In Situ U-Th Disequilibrium Dating Method Utilising Multiple-Spot Femtosecond Laser Ablation-CRC-ICP-MS, Geostand. Geoanal. Res., 46, 589–602, https://doi.org/10.1111/ggr.12458, 2022.

Paul, T. and Fitzgerald, P.: Transmission electron microscopic investigation of fission tracks in fluorapatite, Am. Mineral., 77, 336–344, 1992.

Ravenhurst, C. E., Roden-Tice, M. K., and Miller, D. S.: Thermal annealing of fission tracks in fluorapatite, chlorapatite, manganoanapatite, and Durango apatite: Experimental results, Can. J. Earth Sci., 40, 995–1007, https://doi.org/10.1139/e03-032, 2003.

Ruschel, K., Nasdala, L., Kronz, A., Hanchar, J. M., Többens, D. M., Škoda, R., Finger, F., and Möller, A.: A Raman spectroscopic study on the structural disorder of monazite-(Ce), Miner. Petrol., 105, 41–55, https://doi.org/10.1007/s00710-012-0197-7, 2012.

Seydoux-Guillaume, A. M., Wirth, R., Nasdala, L., Gottschalk, M., Montel, J. M., and Heinrich, W.: An XRD, TEM and Raman study of experimentally annealed natural monazite, Phys. Chem. Miner., 29, 240–253, https://doi.org/10.1007/s00269-001-0232-4, 2002.

Shukoljukov, J. A. and Komarov, A. N.: Tracks of uranium fission in monazite, Bull. Comm. Determ. Absol. Age Geol. Form., Moscow, Akad. Nau, USSR, 20–26, 1970 (in Russian).

Skrzypek, E., Kawakami, T., Hirajima, T., Sakata, S., Hirata, T., and Ikeda, T.: Revisiting the high temperature metamorphic field gradient of the Ryoke Belt (SW Japan): New constraints from the Iwakuni-Yanai area, Lithos, 260, 9–27, https://doi.org/10.1016/j.lithos.2016.04.025, 2016.

Suzuki, K., Kawakami, T., Sueoka, S., Yamazaki, A., Kagami, S., Yokoyama, T., and Tagami, T.: Solidification pressures and ages recorded in mafic microgranular enclaves and their host granite: An example of the world's youngest Kurobegawa granite, Isl. Arc, 31, e12462, https://doi.org/10.1111/IAR.12462, 2022.

Tamer, M. T. and Ketcham, R. A.: The along-track etching structure of fission tracks in apatite: Observations and implications, Chem. Geol., 553, 119809, https://doi.org/10.1016/j.chemgeo.2020.119809, 2020.

Tamer, M. T., Chung, L., Ketcham, R. A., and Gleadow, A. J.W.: Analyst and etching protocol effects on the reproducibility of apatite confined fission-track length measurement, and ambient-temperature annealing at decadal timescales, Am. Mineral., 104, 1421–1435, https://doi.org/10.2138/am-2019-7046, 2019.

Tomiya, A. and Miyagi, I.: Age of the Toya eruption, Bull. Volcanol. Soc. Japan, 65, 13–18, 2020 (in Japanese).

Váczi T.: A new, simple approximation for the deconvolution of instrumental broadening in spectroscopic band profiles, Appl. Spectrosc., 68, 1274–1278, https://doi.org/10.1366/13-07275, 2014.

Warr, L. N.: IMA–CNMNC approved mineral symbols, Mineral. Mag., 85, 291–320, https://doi.org/10.1180/mgm.2021.43, 2021.

Weise, C., van den Boogaart, K. G., Jonckheere, R., and Ratschbacher, L.: Annealing kinetics of Kr-tracks in monazite: Implications for fission-track modelling, Chem. Geol., 260, 129–137, https://doi.org/10.1016/j.chemgeo.2008.12.014, 2009.

Yamada, R.: Cooling history analysis of granitic rock in the northern Alps, central Japan, Earth Mon. (Gekkan Chikyu), 21, 803–810, 1999.

Yamada, R., Tagami, T., and Nishimura, S.: Assessment of overetching factor for confined fission-track length measurement in zircon, Chem. Geol., 104, 251–259, https://doi.org/10.1016/0009-2541(93)90154-B, 1993.

Yamada, R., Tagami, T., and Nishimura, S.: Confined fission-track length measurement of zircon: assessment of factors affecting the paleotemperature estimate, Chem. Geol., 119, 293–306, https://doi.org/10.1016/0009-2541(94)00108-K, 1995.

Yamagata, K.: Tephrochronological Study on the Shikotsu and Kuttara Volcanoes in Southwestern Hokkaido, Japan, J. Geogr. (Chigaku Zasshi), 103, 268–285, https://doi.org/10.5026/jgeography.103.268, 1994.